

Use of a 'caged' analogue to study the traffic of choline within acetylcholinesterase by kinetic crystallography

Jacques-Philippe Colletier,^{a,‡}
Antoine Royant,^{b,c} Alexandre
Specht,^d Benoît Sanson,^a Florian
Nachon,^e Patrick Masson,^e
Giuseppe Zaccai,^{a,f} Joel L.
Sussman,^g Maurice Goeldner,^d
Israel Silman,^h Dominique
Bourgeois^{b,c} and Martin Weik^{a*}

^aLaboratoire de Biophysique Moléculaire, Institut de Biologie Structurale 'Jean-Pierre EBEL', UMR 5075 CNRS-CEA-UJF, 38027 Grenoble, France, ^bLaboratoire de Cristallogénèse et de Cristallographie des Protéines, Institut de Biologie Structurale 'Jean-Pierre EBEL', UMR 5075 CNRS-CEA-UJF, 38027 Grenoble, France, ^cESRF, 6 rue Jules Horowitz, BP 220, 38043 Grenoble Cedex, France, ^dLaboratoire de Chimie Bioorganique, UMR 7175-LC01 CNRS, Faculté de Pharmacie, Université Louis Pasteur, 74 Route du Rhin, 67400 Illkirch, France, ^eUnité d'Enzymologie, Centre de Recherches du Service de Santé des Armées, La Tronche, France, ^fInstitut Laue-Langevin, 6 rue Jules Horowitz, BP 156, 38042 Grenoble, France, ^gDepartment of Structural Biology, Weizmann Institute of Science, 76100 Rehovot, Israel, and ^hDepartment of Neurobiology, Weizmann Institute of Science, 76100 Rehovot, Israel

‡ Present address: UCLA-DOE Institute of Genomics and Proteomics, University of California, Los Angeles, CA 90095-1570, USA.

Correspondence e-mail: weik@ibs.fr

Acetylcholinesterase plays a crucial role in nerve-impulse transmission at cholinergic synapses. The apparent paradox that it displays high turnover despite its active site being buried raises cogent questions as to how the traffic of substrates and products to and from the active site can occur so rapidly in such circumstances. Here, a kinetic crystallography strategy aimed at structurally addressing the issue of product traffic in acetylcholinesterase is presented, in which UV-laser-induced cleavage of a photolabile precursor of the enzymatic product analogue arsenocholine, 'caged' arsenocholine, is performed in a temperature-controlled X-ray crystallography regime. The 'caged' arsenocholine was shown to bind at both the active and peripheral sites of acetylcholinesterase. UV irradiation of a complex with acetylcholinesterase during a brief temperature excursion from 100 K to room temperature is most likely to have resulted in a decrease in occupancy by the caged compound. Microspectrophotometric experiments showed that the caged compound had indeed been photocleaved. It is proposed that a fraction of the arsenocholine molecules released within the crystal had been expelled from both the active and the peripheral sites. Partial *q*-weighted difference refinement revealed a relative movement of the two domains in acetylcholinesterase after photolysis and the room-temperature excursion, resulting in an increase in the active-site gorge volume of 30% and 35% in monomers *A* and *B* of the asymmetric unit, respectively. Moreover, an alternative route to the active-site gorge of the enzyme appeared to open. This structural characterization of acetylcholinesterase 'at work' is consistent with the idea that choline exits from the enzyme after catalysis either *via* the gorge or *via* an alternative 'backdoor' trajectory.

Received 9 January 2007

Accepted 11 September 2007

PDB References: NPT-AsCh-TcAChE complex, 2v96, r2v96sf; 2v97, r2v97sf; 2v98, r2v98sf; native TcAChE, 2va9, r2va9sf.

1. Introduction

Acetylcholinesterase (AChE) terminates nerve-impulse transmission at cholinergic synapses by rapid hydrolysis of the neurotransmitter acetylcholine (ACh; Rosenberry, 1975). This occurs in a two-step reaction: (i) the enzyme is acetylated with concomitant release of choline and (ii) a water molecule regenerates the free enzyme with concomitant release of acetic acid. In accordance with its crucial role, AChE is among the most efficient enzymes, with a turnover of 10^3 – 10^4 s⁻¹ (Quinn, 1987; Silman & Sussman, 2005). It is also the target of a broad repertoire of poisons ranging from organophosphorus and carbamate insecticides (Casida & Quistad, 2005) and nerve agents (Millard & Broomfield, 1995) to natural toxins such as the alkaloid *d*-tubocurarine (Golicnik *et al.*, 2001) and fasciculin (FAS), a polypeptide toxin isolated from mamba

venom (Karlsson *et al.*, 1984). Furthermore, AChE is the target of the first generation of anti-Alzheimer drugs (Greenblatt *et al.*, 2003).

The crystal structure of *Torpedo californica* AChE (TcAChE; Sussman *et al.*, 1991) unexpectedly revealed its active site to be deeply buried near the bottom of a narrow gorge. The enzyme is composed of two domains (Morel *et al.*, 1999) which face one another across the active-site gorge (Fig. 1). In addition to the active site, there is a second substrate-binding site, the peripheral anionic site (PAS), near the entrance to the gorge (Fig. 1; Colletier *et al.*, 2006). At the active site, the choline moiety of ACh is principally stabilized by a cation– π interaction with the indole ring of Trp84 (the residue numbering throughout the manuscript is that of TcAChE), but also interacts with Glu199 and Phe330. The acetyl moiety also contributes to substrate stabilization in the active site by interactions of its carbonyl O atom and its methyl group with the ‘oxyanion hole’ (Gly117, Gly118 and Ala201) and the ‘acyl pocket’ (Trp233, Phe288, Phe290 and Phe331), respectively (Harel *et al.*, 1996; Colletier *et al.*, 2006). The catalytic triad, which is typical of a serine hydrolase, comprises Ser200, His440 and Glu327. The principal residues contributing to the PAS are Trp279, Tyr70, Tyr121 and Asp72. Site-directed mutagenesis, kinetic studies using PAS and catalytic anionic site (CAS) inhibitors (Radic *et al.*, 1991, 1994, 1995; Eichler *et al.*, 1994; Barak *et al.*, 1994; Golicnik *et al.*, 2001) and crystallographic studies of inhibitor–AChE complexes (Harel *et al.*, 1993; Bourne *et al.*, 1995; Harel *et al.*, 1995; Felder *et al.*, 2002) have produced a clear picture of the functional and structural architecture of the active-site gorge. Recently, X-ray crystallography has revealed structural details of substrate and product binding at both the CAS and the PAS (Colletier *et al.*, 2006; Bourne *et al.*, 2006).

The sequestration of its active site raises cogent questions as to how AChE achieves its high rate of substrate turnover. The narrowness of the gorge, which is only 5 Å wide at a bottleneck formed by the van der Waals surfaces of Phe330 and Tyr121, implies that AChE must undergo significant ‘breathing’ motions for traffic of substrates and products to occur *via* this route (Shen *et al.*, 2002; Xu *et al.*, 2003). Aligned with the gorge is a strong electrostatic gradient (Ripoll *et al.*, 1993; Felder *et al.*, 2002) that seems to be involved in guidance of the positively charged ACh towards the active site. However, this gradient should also impede the exit of the product choline (Ch). In this context, an alternative ‘backdoor’ exit for Ch was proposed (Ripoll *et al.*, 1993; see also Axelsen *et al.*, 1994), supporting evidence for which was obtained by molecular-dynamics (MD) simulations (Gilson *et al.*, 1994). This putative backdoor, which was not identified in the static X-ray structure, was reported to be adjacent to the Ch-binding locus of the CAS, Trp84. Likewise, an exit trajectory for the second product, acetate, was proposed just behind the ‘acyl pocket’ (Kovach *et al.*, 1994) and involves the 279–290 loop, which is seen to be disordered in the crystal structure of a TcAChE–galanthamine derivative complex (Greenblatt *et al.*, 2004). Further experimental evidence for alternative access and exit routes to and from the active site comes from the absence of a

bulky leaving group in the crystal structure of TcAChE conjugated with a gorge-filling inhibitor covalently linked to Ser200 (Bartolucci *et al.*, 1999) and from the residual catalytic activity observed for AChE in complex with the gorge-capping polypeptide toxin fasciculin (FAS; Marchot *et al.*, 1993; Eastman *et al.*, 1995; Radic *et al.*, 1994, 1995). Subsequent MD studies have provided further evidence for a repertoire of ‘backdoors’ and ‘side doors’ (see, for example, Wlodek *et al.*, 1997; Enyedy *et al.*, 1998; Tai *et al.*, 2001; Bui *et al.*, 2004). However, mutagenesis studies have not yet provided any supporting evidence for a functional backdoor (Kronman *et al.*, 1994; Velan *et al.*, 1996; Faerman *et al.*, 1996). In this study, we used kinetic crystallography in an attempt to visualize the routes of product traffic within AChE.

In contrast to conventional X-ray crystallography, kinetic crystallography aims to describe the structural changes of crystalline proteins ‘in action’ (reviewed by Hajdu & Andersson, 1993; Bourgeois & Royant, 2005). It is important to note that many proteins are active in the crystalline state (Mozzarelli & Rossi, 1996), since a large amount of conformational freedom is preserved (Nienhaus *et al.*, 1998). Several kinetic crystallography approaches have been described based on real-time monitoring, steady-state accumulation or trapping of rate-limited intermediate states. Common to all these approaches is the requirement for reaction initiation in the crystal, *e.g.* by substrate delivery, pH jump or, in the case of photosensitive samples, by laser or flash-lamp irradiation. Reaction triggering by light is usually applied to proteins possessing endogenous photosensitivity such as haem proteins or photoreceptors. For proteins that are not innately photosensitive, use can be made of so-called ‘caged compounds’; for example, photosensitive precursors of enzyme substrates or products (Schlichting *et al.*, 1990; Hajdu & Andersson, 1993;

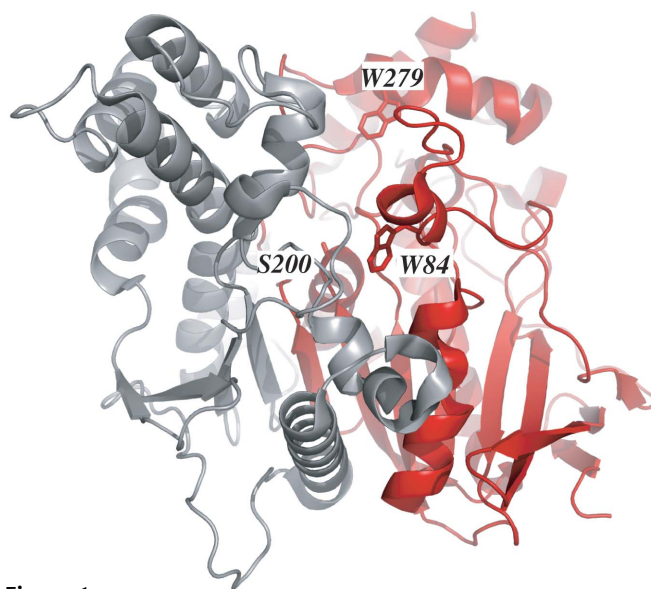


Figure 1 Three-dimensional structure of TcAChE, highlighting the two domains on either side of the active-site gorge (residues 4–305 in red, residues 306–535 in grey). The catalytic Ser200 and Trp84 are shown at the bottom of the gorge (CAS) and the peripheral-site Trp279 at its rim (PAS).

Scheidig *et al.*, 1999; Ursby *et al.*, 2002; Bourgeois & Weik, 2005).

Here, we report kinetic crystallography studies on *TcAChE* that combine temperature-controlled crystallography and the use of a 'caged' precursor of an analogue of the product Ch, arsenocholine (AsCh; Specht & Goeldner, 2004). Photolysis of the 'caged' compound was achieved by means of laser irradiation at room temperature (RT) during a brief temperature excursion from 100 K to RT. Partial *q*-weighted difference refinement (Fermi *et al.*, 1982; Terwilliger & Berendzen, 1995; Ursby & Bourgeois, 1997) was performed, which allowed the characterization of an activated state of the enzyme. The data suggest that the transient temperature increase to RT and photolysis resulted in reduced occupancy of AsCh at both the CAS and the PAS. Concomitantly, conformational changes were detected in the active-site gorge of the activated-state model of *TcAChE* which resulted in the increase of the gorge volume and in the opening of an alternative route to and/or from the active site that may be involved in clearance of Ch from the active site.

2. Experimental procedures

2.1. Caged compound

The iodide salt of the caged compound [1-(2-nitrophenyl)-2,2,2-trifluoroethyl]-arsenocholine (NPT-AsCh; Fig. 2) was synthesized as described by Specht & Goeldner (2004). Its K_i for *TcAChE* is 29 μM in 25 mM sodium phosphate pH 7.0 at 293 K (J.-P. Colletier, unpublished results). When dissolved in water, NPT-AsCh displays an absorption maximum at 263 nm (not shown). The *o*-nitrosotrifluoromethylacetophenone released by UV irradiation has an absorption peak at 320 nm (not shown). Thus, photocleavage of NPT-AsCh can be monitored spectrophotometrically by following either its disappearance or the appearance of the byproduct. However, when it is complexed with crystalline *TcAChE* the absorption of the latter at 280 nm prevents monitoring of the disappearance of NPT-AsCh and only the appearance of *o*-nitrosotrifluoromethylacetophenone can be monitored. The molar extinction coefficient of NPT-AsCh at 266 nm is 5160 $\text{M}^{-1} \text{cm}^{-1}$ and that of the free cage is 4200 $\text{M}^{-1} \text{cm}^{-1}$ at 320 nm.

2.2. Crystallization of *TcAChE*, choice of crystal form and soaking procedure

TcAChE was purified as described previously (Sussman *et al.*, 1988; Raves, 1998). Orthorhombic $P2_12_12_1$ (Greenblatt *et al.*, 2004) and trigonal $P3_121$ (Sussman *et al.*, 1991) crystals of native *TcAChE* were obtained at 277 K by the hanging-drop vapour-diffusion method under the same crystallization conditions. The mother liquor was 32% PEG 200, 0.15 M MES pH 5.8–6.2 and a protein concentration of 11.5 mg ml^{-1} was employed. Orthorhombic *TcAChE*

crystals grew as thin plates (typically $150 \times 150 \times 50 \mu\text{m}$) and were thus preferred over the more chunky trigonal crystals in order to maximize the penetration of UV light throughout the crystal. In order to obtain the crystalline NPT-AsCh–*TcAChE* complex, orthorhombic crystals were soaked in the dark for 12 h at 277 K in mother liquor containing 5 mM NPT-AsCh pH 6.0. Crystals were washed for 10 s in mother liquor devoid of NPT-AsCh before flash-cooling to 100 K in a stream of gaseous N_2 . Owing to the cryoprotective capacity of PEG 200, no additional cryoprotectant was necessary.

2.3. Cryophotolysis and microspectrophotometry

All microspectrophotometric characterization and preliminary experiments were conducted at the Cryobench Laboratory, which is jointly maintained by the European Synchrotron Radiation Facility (ESRF) and the Institut de Biologie Structurale (IBS) (Bourgeois *et al.*, 2002), and where a microspectrophotometer permits direct absorption measurements at 200–850 nm by protein crystals or by small solution volumes. The apparatus is composed of (i) a one-circle goniometer, (ii) three identical confocal mirror objectives focusing/collecting UV–visible light to/from the crystal, (iii) a CCD spectrophotometer (2.3 nm resolution in the 200–850 nm range, Ocean Optics), (iv) a microscope (Olympus) connected to a high-resolution camera (Olympus) permitting observation and centring of the crystal and (v) a cryocooling device (Oxford Cryosystems 600) that allows both flash-cooling and subsequent application of desired temperature profiles. Two of the objectives are aligned for transmission mode, while the third one is at 90° and is used to focus a 266 nm laser (2 mW passively *q*-switched YAG laser; Nanolase) onto the crystal. The laser and a deuterium/halogen lamp (Micropack deuterium/halogen lamp; Ocean Optics) are connected to the focusing objectives using optical fibres of 600 and 100 μm diameter (Spectraline), respectively, while an optical fibre of 200 μm diameter is used to guide the light from the receiving objective to the spectrophotometer. Spectra were recorded and analysed on a PC using the *OOIBase32* software package (Ocean Optics). A detailed description of the Cryobench Laboratory can be found at <http://www.esrf.fr/UsersAndScience/Experiments/MX/Cryobench/> (see also Bourgeois *et al.*, 2002; Royant *et al.*, 2007). To minimize ambient light exposure, which might produce small but unquantifiable photolysis of NPT-AsCh, the Cryobench Laboratory was only lit by a sodium lamp throughout all the experiments. Fig. 3(a) shows an experiment performed on an orthorhombic *TcAChE* crystal soaked for 12 h in the dark at

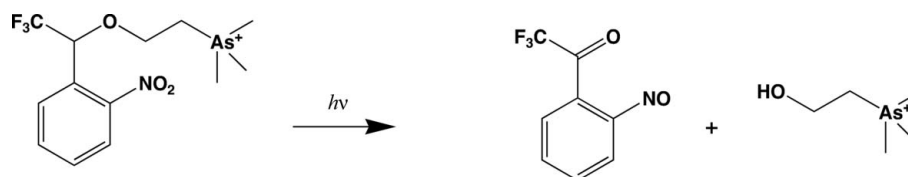


Figure 2
Photocleavage of NPT-AsCh into AsCh and *o*-nitrosotrifluoromethylacetophenone.

Table 1

Data-collection and refinement statistics.

Values in parentheses are for the highest resolution shells.

	Unphotolysed NPT-AsCh–TcAChE complex (structure 1)	Unphotolysed NPT-AsCh–TcAChE complex after ART (structure 2)	UV-damaged native TcAChE (structure 3)	NPT-AsCh–TcAChE complex after photolysis and annealing to RT (structure 4)
PDB code	2v96	2v97	2va9	2v98
ESRF beamline	BM30A	ID14-EH4	ID14-EH4	ID14-EH4
Data-collection temperature (K)	100	100	100	100
Oscillation step (°)	1	1	1	1
No. of frames	150	120	120	120
Exposure time per frame (s)	30	1	1	1
Wavelength (Å)	0.977	0.932	0.932	0.932
Space group	<i>P</i> 2 ₁ 2 ₁ 2 ₁	<i>P</i> 2 ₁ 2 ₁ 2 ₁	<i>P</i> 2 ₁ 2 ₁ 2 ₁	<i>P</i> 2 ₁ 2 ₁ 2 ₁
Unit-cell parameters (Å)				
<i>a</i>	91.42	91.20	91.42	91.62
<i>b</i>	103.64	104.46	106.55	104.47
<i>c</i>	147.31	148.05	150.15	148.80
Mosaicity† (°)	0.279	0.352	0.213	0.491
Resolution range (Å)	20.00–2.40 (2.50–2.40)	20.00–2.40 (2.50–2.40)	20.00–2.40 (2.50–2.40)	20.00–3.00 (3.10–3.00)
Completeness (%)	99.1 (99.7)	99.8 (100)	99.6 (97.7)	96.6 (94.6)
<i>R</i> _{merge} ‡ (%)	7.9 (34.7)	10.7 (46.7)	12.4 (45.0)	12.6 (49.8)
<i>I</i> / σ (<i>I</i>)	15.4 (4.4)	8.4 (2.8)	9.7 (3.1)	8.84 (2.5)
Unique reflections	54936	55871	58043	29073
Redundancy	5.9	3.8	6.1	3.3
<i>R</i> _{cryst} (%)	20.9	20.5§	20.4	20.3§
<i>R</i> _{free} (%)	24.4	26.7§	24.7	24.9§
R.m.s.d. bond lengths (Å)	0.009	0.007	0.006	0.009
R.m.s.d. bond angles (°)	1.501	1.535	1.326	1.415
No. of atoms in ASU				
Protein	8610	8455	8455	8455
Water	989	1083	855	1083
Carbohydrate	56	56	56	56
Ligands	84	84	0	84
Wilson <i>B</i> factor (Å ²)	36.35	41.82	31.13	47.81
Average <i>B</i> factor (Å ²)	34.39	38.82	21.40	42.36
Protein	33.39	36.03¶, 37.69††	29.02	41.83‡‡, 40.02§§
R.m.s.d. <i>B</i>				
Bonds				
Main-chain atoms	1.088	1.222	1.193	0.927
Side-chain atoms	1.706	1.908	1.879	1.142
Angles				
Main-chain atoms	1.815	1.979	1.924	1.585
Side-chain atoms	2.520	2.805	2.759	1.709
Water	41.38	51.85¶, 51.60††	38.27	52.86‡‡, 50.70§§
Carbohydrate	51.27	59.00¶, 58.61††	49.09	55.52‡‡, 58.94§§
Ligands	41.37	53.50¶, 56.22††	n/a	51.48‡‡, 55.65§§
Ramachandran statistics (%)				
Core	87.4	87.7¶, 80.4††	87.5	87.7‡‡, 76.7§§
Allowed regions	11.8	11.8¶, 18.4††	11.5	11.8‡‡, 21.9§§
Generously allowed regions	0.8	0.4¶, 1.0††	0.9	0.4‡‡, 1.1§§
Disallowed regions	0	0¶, 0††	0.1	0.0‡‡, 0.2§§

† Mosaicity as determined by XDS (Kabsch, 1993). ‡ $R_{\text{merge}} = 100 \sum_{hkl} \sum_i |I_i(hkl) - \langle I(hkl) \rangle| / \sum_{hkl} \sum_i I_i(hkl)$. § See Table 3 for details of *R* and *R*_{free} of structures 2 and 4. ¶ Value for structure 2^{GS}. †† Value for structure 2^{AS}. ‡‡ Value for structure 4^{GS}. §§ Value for structure 4^{AS}.

277 K in 5 mM NPT-AsCh solution in mother liquor at pH 6.0. The crystal was then washed for 10 s in mother liquor devoid of NPT-AsCh before being loop-mounted and flash-cooled to 100 K. Fig. 3(a) shows the difference absorption spectra recorded at 100 K across the crystal after 300, 400, 500, 600, 700, 800 and 900 s exposure to the 266 nm laser. To maximize the efficiency of photolysis, the crystal was rotated during exposure to the laser beam, but all spectra were recorded at the same crystal orientation. Either a 355 nm laser or a flash-lamp could have been used to perform photolysis rather than the 266 nm laser that was actually employed (Specht *et al.*,

2001), but we did not have access to either of these light sources at the time of our experiments. Fig. 3(b) shows a simulation of the 266 nm light transmission across orthorhombic native TcAChE and NPT-AsCh–TcAChE crystals. The concentration of the enzyme in the orthorhombic crystals was calculated to be 9.4 mM. Values for the extinction coefficients of aromatic residues (Trp, Tyr and Phe) at 266 nm were taken from <http://omlc.ogi.edu/spectra/PhotochemCAD/html/index.html> and molar extinction coefficients of 87 339 and 97 659 M⁻¹ cm⁻¹ at 266 nm were calculated for a TcAChE monomer and for a TcAChE monomer in complex with two

NPT-AsCh molecules, respectively. Fig. 3 was produced using the software *PLOT* (<http://plot.micw.eu/>). To ensure efficient photolysis, illumination from two sides or rotation of the crystal during illumination should be performed and the crystal thickness should ideally not exceed $\sim 20\ \mu\text{m}$.

2.4. X-ray data collection

All X-ray data sets were collected at the ESRF after flash-cooling and maintaining the crystal in a stream of gaseous N_2 at 100 K. The data were indexed, merged and scaled using *XDS/XSCALE*. Structure-factor amplitudes were generated using *XDSCONV* (Kabsch, 1993). Data-collection statistics are given in Table 1.

2.4.1. Structure of the unphotolysed NPT-AsCh–TcAChE complex (structure 1). Data were collected to $2.4\ \text{\AA}$ resolution on beamline BM30A (CRG FIP) from a $150 \times 150 \times 50\ \mu\text{m}$ orthorhombic crystal.

2.4.2. Procedure for annealing to room temperature (ART). In order to evaluate the accessible time range for ART, preliminary experiments were conducted ‘in-house’ on a Rigaku R-AXIS IV diffractometer using native TcAChE crystals. Typical dimensions of orthorhombic and trigonal crystals of TcAChE are $150 \times 150 \times 50$ and $150 \times 150 \times 150\ \mu\text{m}$, respectively. Crystals were mounted in a cryo-loop and flash-cooled to 100 K. After an initial diffraction image had been collected, ART was carried out by manually blocking the N_2 -gas stream with a card for 1–60 s. After termination of ART, a second diffraction image was collected at 100 K and its diffraction limit was compared with that of the first image. Permissible time ranges for ART, *i.e.* the time during which no loss in the diffraction limit was observed, were ≤ 45 s for orthorhombic crystals and ≤ 30 s for trigonal crystals. The time spans required for crystals to reach RT were found to be 4 and 7 s for the orthorhombic and trigonal crystal forms, respectively, as evidenced by the absence of ice rings in the second diffraction pattern. Recovery of the diffraction power after the ART procedure is highly reproducible for crystals of either type (as assessed more than ten times on native TcAChE

crystals and more than 20 times on the complexes of various substrates, products or ligands with TcAChE in both the orthorhombic and the trigonal crystal forms). However, trigonal crystals are more sensitive to multiple annealing cycles than orthorhombic crystals; while up to ten ART cycles of 5 s each can be undergone by a typical orthorhombic crystal without loss of more than $0.5\ \text{\AA}$ resolution, for trigonal crystals the second round of annealing is often already detrimental. The fact that the diffraction power of native orthorhombic crystals is occasionally increased upon ART is noteworthy.

2.4.3. Effect of ART on the structure of the unphotolysed NPT-AsCh–TcAChE complex (structure 2). The effect of ART on the structure of the unphotolysed NPT-AsCh–TcAChE complex was investigated using a $150 \times 150 \times 50\ \mu\text{m}$ orthorhombic crystal. Subsequent to flash-cooling, the crystal underwent ART for 9 s before being flash-cooled back to 100 K for data collection ($2.4\ \text{\AA}$ resolution) on beamline ID14-EH4.

2.4.4. UV damage at RT to a native TcAChE crystal (structure 3). Since our experimental approach involves the use of a 266 nm laser to photocleave NPT-AsCh (see Fig. 4), a control was needed to discriminate between structural changes arising from UV damage at RT and those related to the exit of the NPT-AsCh photolysis products from the active site of TcAChE. To ensure full penetration of the 266 nm light (see Fig. 3*b*), a rather thin orthorhombic crystal ($\sim 250 \times 100 \times 30\ \mu\text{m}$) was employed. The 266 nm laser was connected by a $600\ \mu\text{m}$ optic fibre to the focusing lens of an online microspectrophotometer (Nanao & Ravelli, 2006; Ravelli, Murray, McGeehan, Owen, Cipriani, Theveneau, Weik & Garman, manuscript in preparation) centred on the crystal (spot size on the crystal: $150\ \mu\text{m}$). The crystal was brought to RT for 9 s by blocking the cryostream manually with a card, during the first 5 s of which laser irradiation took place, before being flash-cooled back to 100 K for data collection ($2.4\ \text{\AA}$ resolution); thus, a relaxation time of 4 s at RT was allowed after extinction of the laser. The crystal was rotated during the course of exposure to the laser beam.

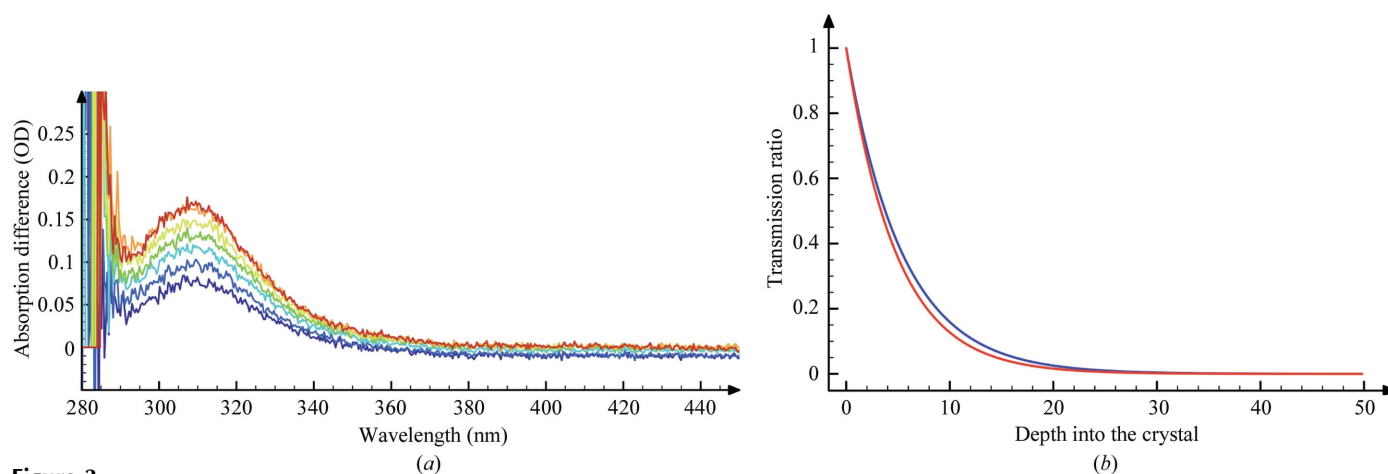


Figure 3 (a) *In crystallo* photolysis of NPT-AsCh. Difference OD spectra were recorded across orthorhombic TcAChE–NPT-AsCh crystals at 100 K after 300, 400, 500, 600, 700, 800 and 900 s (blue to red colour) exposure to a 266 nm laser. (b) Simulated transmission of 266 nm light across orthorhombic native TcAChE (blue) and NPT-AsCh–TcAChE (red) crystals.

2.4.5. Structure of the photolysed NPT-AsCh–TcAChE complex after ART (structure 4). Fig. 4 shows a schematic representation of the experimental procedure. The experiment was performed on beamline ID14-EH4. An orthorhombic crystal of the NPT-AsCh–TcAChE complex of dimensions $\sim 100 \times 100 \times 30 \mu\text{m}$ was employed. Photolysis of the NPT-AsCh was achieved using the experimental setup described in §2.4.4. The experimental procedure was identical to that described above for structure 3.

2.5. Structure determination and refinement

2.5.1. NPT-AsCh–TcAChE complexes. The native structure of TcAChE in the orthorhombic space group (PDB code 1w75; Greenblatt *et al.*, 2004) without sugar and water molecules served as the starting model for rigid-body refinement of the two unphotolysed NPT-AsCh–TcAChE complexes (structures 1 and 2) in the resolution range 20–4 Å. Subsequently, both structures underwent simulated annealing to 2000 K, with slow-cooling steps of 10 K followed by 250 steps of conjugate-gradient minimization. Diffraction data from 20 to 2.4 Å were used for refinement and electron-density map calculations. For both structures, localization and attribution of the NPT-AsCh molecules was rather straightforward since the initial electron-density maps were of good quality. For each of the two monomers in the asymmetric unit (*A* and *B*) two NPT-AsCh molecules were assigned with full occupancies: one at the CAS and one at the PAS (Fig. 5). The strong

Table 2

R_{free} and R values for structure 4 after various refinement procedures.

	Complete independent refinement	Difference refinement†	<i>q</i> -weighted difference refinement	<i>q</i> -weighted partial (20%) difference refinement
R_{free} (%)	31.9	33.0	32.3	31.7
R_{\ddagger} (%)	28.3	29.3	29.5	23.0
$R_{\text{free,diff}}$ (%)		28.6	25.3	24.9
R_{diff} (%)		23.9§	20.2¶	20.3¶

† Both sets of R factors are given here, *i.e.* the standard R/R_{free} factors and the difference $R_{\text{diff}}/R_{\text{free,diff}}$ factors. However, for assessing the accuracy of the difference refinement, only R_{diff} and $R_{\text{free,diff}}$ are relevant (Terwilliger & Berendzen, 1995). ‡ $R = 100 \sum_{hkl} ||F_{\text{obs},4}(hkl) - |F_{\text{calc},4}(hkl)|| / \sum_{hkl} |F_{\text{obs},4}(hkl)|$. § $R_{\text{diff}} = 100 \sum_{hkl} ||F_{\text{calc},2}(hkl) + |F_{\text{obs},4}(hkl)| - |F_{\text{obs},2}(hkl)|| / \sum_{hkl} ||F_{\text{calc},2}(hkl) + |F_{\text{obs},4}(hkl)| - |F_{\text{obs},2}(hkl)||$. ¶ $R_{\text{diff}}^q = 100 \sum_{hkl} ||F_{\text{calc},2}(hkl) + q||F_{\text{obs},4}(hkl)| - |F_{\text{obs},2}(hkl)|| - |F_{\text{calc},4}(hkl)|| / \sum_{hkl} ||F_{\text{calc},2}(hkl) + q||F_{\text{obs},4}(hkl)| - |F_{\text{obs},2}(hkl)||$.

anomalous signal of the As atom permitted unequivocal determination of the position of the AsCh moieties of the NPT-AsCh molecules (anomalous peaks of height $>17\sigma$ at both binding loci in both structures 1 and 2). *CNS* composite $2F_o - F_c$ OMIT maps were calculated, which provided the basis for the first step of manual rebuilding. Atoms lacking density at 1σ in this map were not included in the initial model and were reattributed afterwards only if subsequent $F_o - F_c$ electron-density maps displayed peaks of $>3\sigma$. Graphic operations and model building were performed with *Coot* (Emsley & Cowtan, 2004). Energy minimization and restrained individual *B*-factor refinement followed each stage of manual rebuilding. Refinement and map calculations were performed using *CNS* v.1.1 (Brünger *et al.*, 1998) and the *REFMAC* (Murshudov *et al.*, 1997) and *FFT* modules of the *CCP4* suite (Collaborative Computational Project, Number 4, 1994).

In order to address the differences between structures 4 and 2, the difference-refinement strategy was employed, *i.e.* refinement using $F_{\text{diff}}^2 = F_c^2 + (F_o^4 - F_o^2)$ (Fermi *et al.*, 1982; Terwilliger & Berendzen, 1995). *q*-weights (Ursby & Bourgeois, 1997), which improve the estimate of the structure-factor amplitude differences, were used to ameliorate the signal-to-noise ratio [*i.e.* refinement using $F_{\text{diff}}^q = F_c^2 + q \times (F_o^4 - F_o^2)$; see Table 2]. The F_{diff} coefficients used in the refinement of structure 4 were generated using *DATAMAN* (Kleywegt & Jones, 1996) and the *SFTOOLS* module of the *CCP4* suite. In addition, partial refinement was performed to gain further insight into the conformational changes undergone by the NPT-AsCh–TcAChE complex upon UV irradiation and concomitant ART. Partial refinement involves

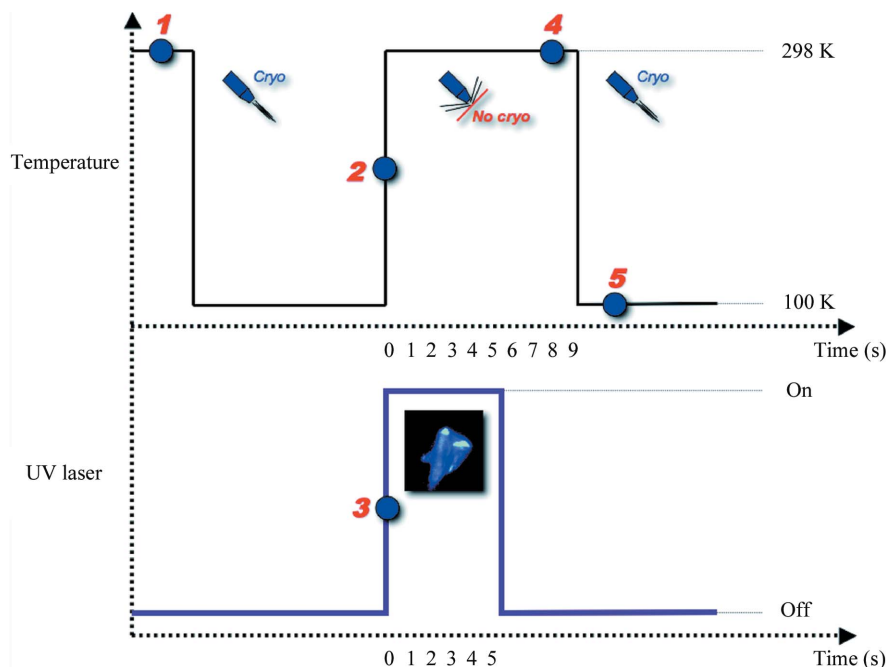


Figure 4 Temperature-controlled protein crystallography combined with photolysis of NPT-AsCh. The photolabile NPT-AsCh binds to the crystalline TcAChE at room temperature (1) and the crystal is then flash-cooled to 100 K in a gaseous stream of N₂. The crystal is then subjected to ART (transient annealing to room temperature; 2), while photodissociation of NPT-AsCh to AsCh and *o*-nitrosotrifluoromethylacetophenone is concomitantly induced by a UV laser (3). Various relaxation times at room temperature are allowed after laser extinction (4). Structural changes of TcAChE related to AsCh exit from the active site can then be trapped and characterized by X-ray data collection at 100 K (5).

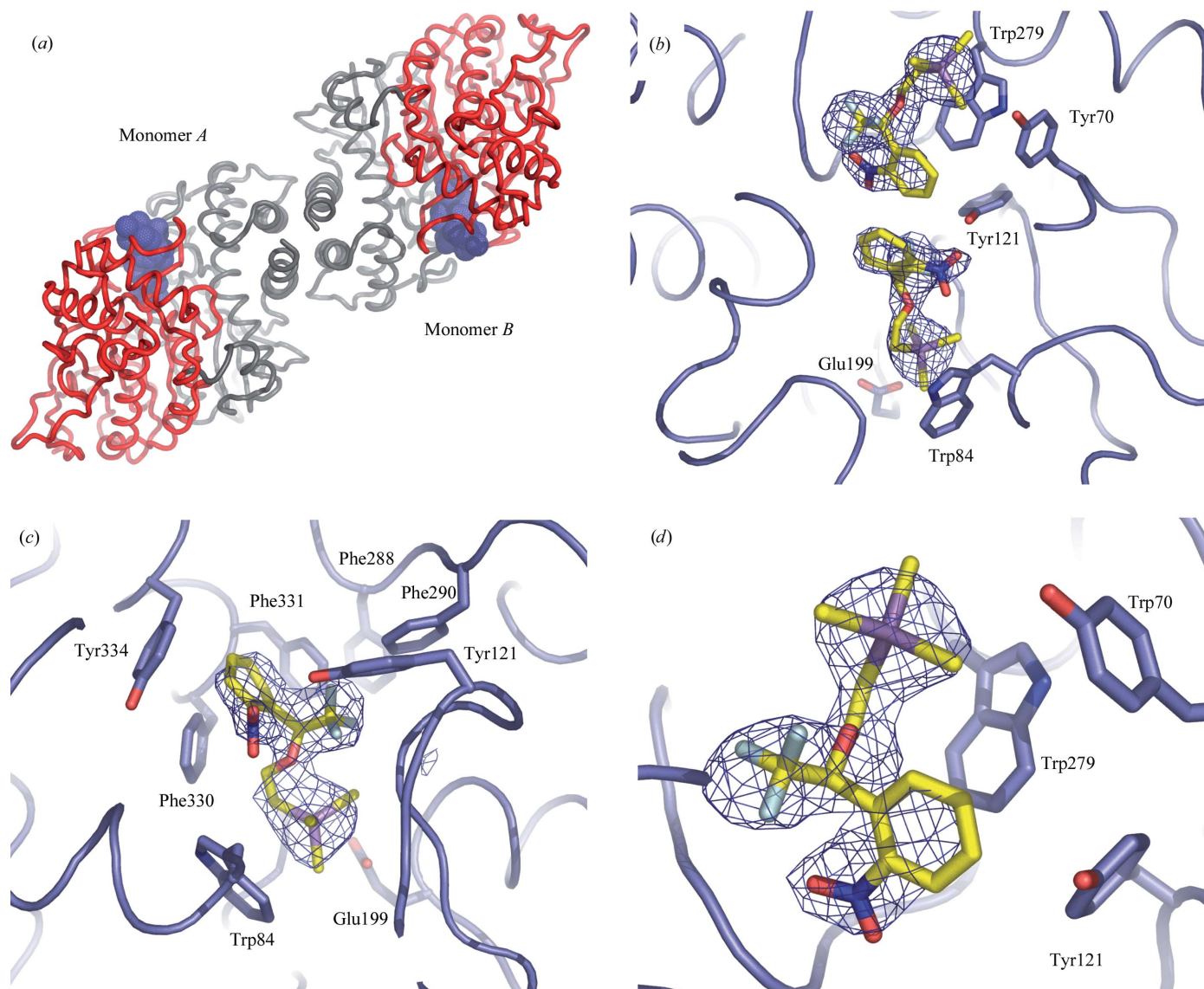
refinement of an 'activated-state' (AS) conformation while the 'ground-state' (GS) model is held fixed. In practice, structure **2** was used as the starting model for rigid-body refinement using F_{diff}^q . Subsequently, two identical models, **4**^{GS} and **4**^{AS}, were generated. Structure **4**^{GS} was held fixed by virtue of a strong harmonic force constant ($418 \text{ kJ mol}^{-1} \text{ \AA}^{-2}$), whereas **4**^{AS} was refined using F_{diff}^q by simulated annealing to 2000 K with cooling steps

Table 3

R_{free} and R values for structure **2** after partial refinement and for structure **4** after partial q -weighted difference refinement.

	Structure 2 before partial refinement	Structure 2 20% AS/ 80% GS	Structure 4 20% AS/ 80% GS	Structure 4 40% AS/ 60% GS	Structure 4 60% AS/ 40% GS	Structure 4 80% AS/ 20% GS	Structure 4 100% AS/ 0% GS
R_{free} (%)	27.2	26.7					
R^{\dagger} (%)	21.1	20.5					
$R_{\text{free,diff}}$ (%)			24.9	25.2	25.6	25.4	25.3
$R_{\text{diff}}^{\ddagger}$ (%)			20.3	20.1	20.0	20.1	20.2

$\dagger R = 100 \sum_{hkl} (|F_{\text{obs},2}(hkl)| - |F_{\text{calc},2}(hkl)|) / \sum_{hkl} |F_{\text{obs},2}(hkl)|$. $\ddagger R_{\text{diff}} = 100 \sum_{hkl} (|F_{\text{calc},2}(hkl)| + q|F_{\text{obs},4}(hkl)| - |F_{\text{obs},2}(hkl)| - |F_{\text{calc},4}(hkl)|) / \sum_{hkl} (|F_{\text{calc},2}(hkl)| + q|F_{\text{obs},4}(hkl)| - |F_{\text{obs},2}(hkl)| - |F_{\text{calc},4}(hkl)|)$, with $F_{\text{calc},4}(hkl) = aF_{\text{calc},4^{\text{GS}}}(hkl) + bF_{\text{calc},4^{\text{AS}}}(hkl)$, where a and b are the fractions of **4**^{GS} and **4**^{AS}, respectively.

**Figure 5**

NPT-AsCh-binding sites in the unphotolysed NPT-AsCh-TcAChE complex (structure **1**). (a) Overview of the dimer constituting the asymmetric unit. The C-terminal domains (in grey) of the two monomers interact with each other *via* a four-helix bundle. The caged compounds bound inside the gorge are shown as blue spheres; the N-terminal domains are shown in red. (b) Overview of the binding sites: Trp84 and Glu199 are shown in the CAS and Tyr70, Tyr121 and Trp279 at the PAS. (c) NPT-AsCh bound in the CAS. Trp84, Glu199 and Phe330 are shown in the CAS, as well as Phe288, Phe290 and Phe331 in the acyl pocket and Tyr334. (d) NPT-AsCh bound at the PAS. The principal PAS residues, Tyr70, Tyr121 and Trp279, are shown. The $F_o - F_c$ electron-density map (contour level 3.5σ) computed without the atomic coordinates of NPT-AsCh is superimposed on the model (monomer **B**) in (b)–(d).

Table 4

R.m.s.d. and maximum-likelihood σ values (\AA) between structures.

The mean value is 0.3 \AA .

	1w75	Structure N	Structure 1	Structure 2 ^{GS}	Structure 2 ^{AS}	Structure 3	Structure 4 ^{GS}	Structure 4 ^{AS}
1w75	0 (0)	0.22 (0.05)	0.35 (0.08)	0.34 (0.06)	0.46 (0.08)	0.19 (0.04)	0.36 (0.08)	0.65 (0.14)
Structure N	0.22 (0.05)	0 (0)	0.38 (0.07)	0.38 (0.09)	0.48 (0.11)	0.18 (0.04)	0.39 (0.09)	0.68 (0.15)
Structure 1	0.35 (0.08)	0.38 (0.07)	0 (0)	0.23 (0.05)	0.41 (0.06)	0.35 (0.06)	0.29 (0.06)	0.63 (0.14)
Structure 2 ^{GS}	0.34 (0.06)	0.38 (0.08)	0.23 (0.05)	0 (0)	0.38 (0.06)	0.38 (0.09)	0.21 (0.04)	0.58 (0.13)
Structure 2 ^{AS}	0.46 (0.08)	0.48 (0.11)	0.41 (0.06)	0.38 (0.06)	0 (0)	0.46 (0.08)	0.40 (0.07)	0.66 (0.14)
Structure 3	0.19 (0.04)	0.18 (0.04)	0.35 (0.06)	0.38 (0.09)	0.46 (0.08)	0 (0)	0.39 (0.09)	0.68 (0.15)
Structure 4 ^{GS}	0.36 (0.08)	0.39 (0.09)	0.29 (0.06)	0.21 (0.04)	0.40 (0.07)	0.39 (0.09)	0 (0)	0.58 (0.13)
Structure 4 ^{AS}	0.65 (0.14)	0.68 (0.15)	0.63 (0.14)	0.58 (0.13)	0.66 (0.14)	0.68 (0.15)	0.58 (0.13)	0 (0)

of 10 K, conjugate-gradient minimization and restrained individual B -factor refinement. This procedure was carried out five times, with the relative occupancies of 4^{GS} and 4^{AS} being varied from 0% to 100% in steps of 20%; the lowest R_{free} value was obtained for 20% AS and 80% GS (Tables 2 and 3). The resulting $F_o - F_c$ electron-density map is virtually featureless when displayed at $\pm 3\sigma$. As a control, the same partial refinement procedure was then applied to structure 2, the final model of which obtained as described above was used to generate two conformers, 2^{GS} and 2^{AS}, with relative occupancies of 80% and 20%, respectively. While structure 2^{GS} was held fixed by virtue of a strong harmonic force constant ($418 \text{ kJ mol}^{-1} \text{ \AA}^{-2}$), 2^{AS} was subjected to simulated annealing to 2000 K with cooling steps of 10 K, conjugate-gradient

minimization and restrained individual B -factor refinement. Structures 2^{GS} and 2^{AS} are virtually identical to structure 2, yet structure 2^{AS} displays small conformational changes that most probably reflect the conformational heterogeneity of the crystalline sample subsequent to ART. In the case of structure 2, the partial refinement strategy also led to a significant decrease in the R_{free} and R values (Table 3).

Structural differences between structures 1, 2^{GS}, 2^{AS}, 4^{GS} and 4^{AS} were evaluated on the basis of error-scaled difference distance matrices (ESDDM), which were produced using *ESDMM* (Schneider, 2000; Fig. 6) after the maximum-likelihood superpositioning of all structures (1, 2^{GS}, 2^{AS}, 4^{GS} and 4^{AS}; Table 4 and Fig. 7) using *THESEUS* (Theobald & Wuttke, 2006; <http://www.theseus3d.org/>). Owing to the limited resolution of structure 4 and the high correlation between occupancy and B factors, no attempt was made to determine the post-photolysis occupancies of the NPT-AsCh molecules in this structure. Instead, a qualitative assessment was obtained by computing $F_o^4 - F_o^2$ (not shown) and $q \times (F_o^4 - F_o^2)$ difference electron-density maps (Fig. 8; shown only

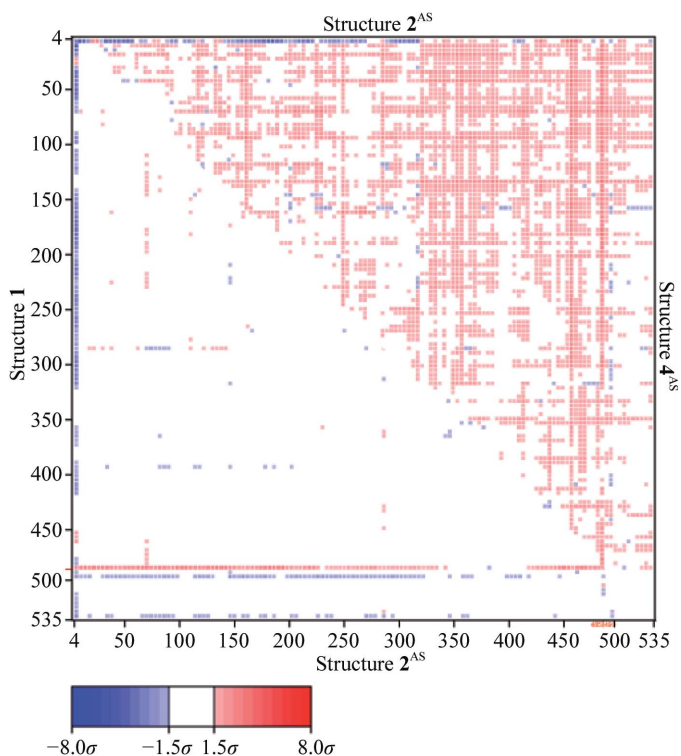


Figure 6
Error-scaled distance difference matrix (ESDDM) between the C^α atoms of structures 1 and 2^{AS} (lower half) and between those of structures 2^{AS} and 4^{AS} (upper half). The ESDDM is shown for monomer A. Red and blue pixels indicate increases and decreases, respectively, in the distances between C^α atoms in structures 1 and 4^{AS} with respect to structure 2^{AS}.

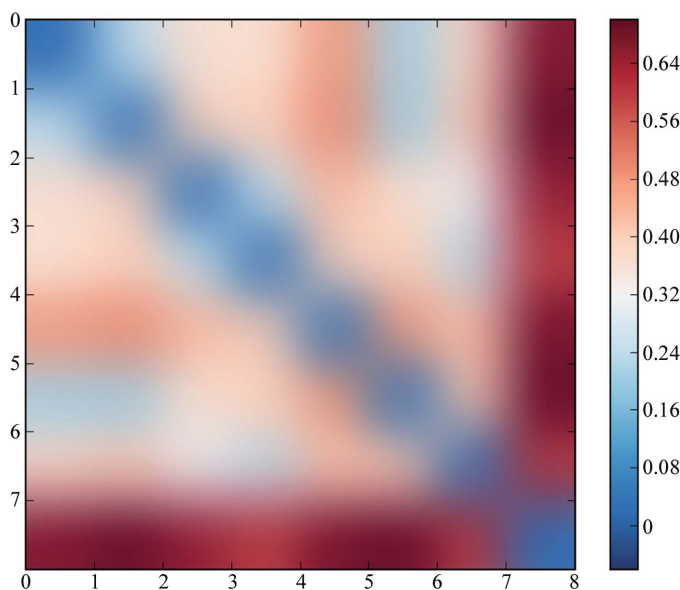


Figure 7
Matrix representation of the r.m.s.d. along the structures (monomers A and B) presented in the manuscript (as listed in Table 4). The blue-to-red scale varies from 0 to 0.70 \AA . Structures are ordered as in Table 4.

Table 5

Molecular volume (\AA^3) of the active-site gorge in native orthorhombic *TcAChE* and in structures **N**, **1**, **2^{GS}**, **2^{AS}**, **3**, **4^{GS}** and **4^{AS}**.

Mean volume of the active-site gorge in native *TcAChE* (structures 1w75, **N** and **3**): 915 \AA^3 (monomer *A*) and 929 \AA^3 (monomer *B*).

	1w75	Structure N	Structure 1	Structure 2^{GS}	Structure 2^{AS}	Structure 3	Structure 4^{GS}	Structure 4^{AS}
Monomer <i>A</i>	911	937	885	955	935	896	911	1177
Monomer <i>B</i>	904	963	925	977	1004	920	927	1247

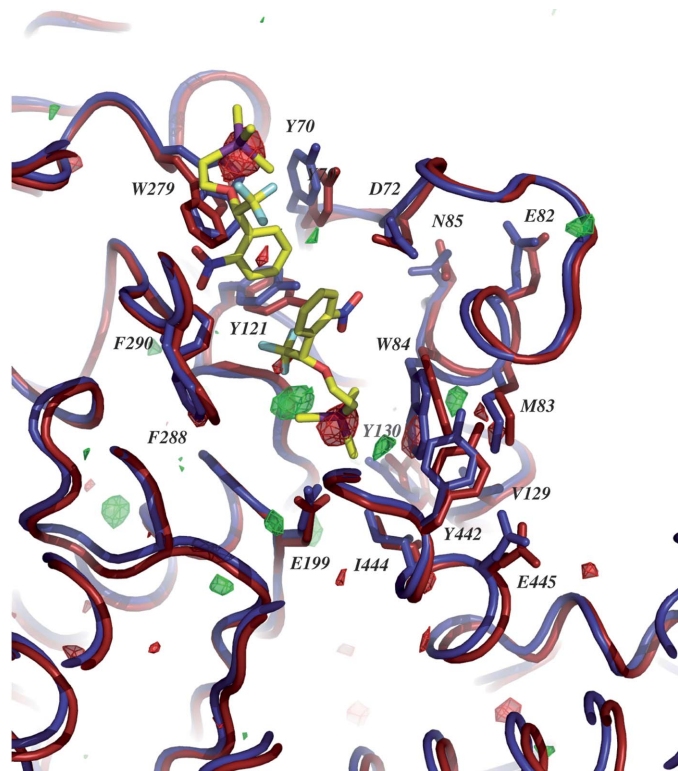


Figure 8

Relative decreases in the occupancies of NPT-AsCh in monomer *A* of structure **4** relative to structure **2**. The C^{α} traces of structures **2^{GS}** and **4^{AS}** are shown in dark blue and red, respectively. Residues Asp72, Trp84, Tyr130, Glu199 and Phe290 in the CAS and Tyr70, Tyr121 and Trp279 at the PAS are shown for both structures. Residues in the putative backdoor region (Met83, Val129, Tyr442, Ile444 and Glu445) are also shown. The $q \times (F_o^4 - F_o^2)$ difference electron-density map is superimposed on the model (contour levels -4σ , red; $+4\sigma$, green).

for monomer *A*) phased with the model of structure **2**. Both difference maps displayed strong negative ($< -5\sigma$) peaks for the As atoms of the two NPT-AsCh molecules bound to each of the two monomers of the asymmetric unit. The $q \times (F_o^4 - F_o^2)$ difference map yielded additional peaks on the protein moiety, which are consistent with the observed differences between structures **2^{AS}** and **4^{AS}**. Figs. 1, 5, 8 and 9 were produced using *PyMOL* (DeLano, 2002). Fig. 6 was produced using *ESCKET* (Schneider, 2000) and Fig. 7, which is a matrix representation of the r.m.s.d. between the structures discussed throughout the manuscript, was produced using a Python script written by Chris Miller. Molecular topologies and parameters of NPT-AsCh were created using *XPLOR2D*

(Kleywegt, 1995). The qualities of the structures were checked and validated using *PROCHECK* (Laskowski *et al.*, 1993) from the *CCP4* suite. The molecular volumes of the active-site gorge in the various structures were computed using *CASTp* (Dundas *et al.*, 2006) and are presented in Table 5. Refinement statistics are displayed in Table 1.

2.5.2. UV-damaged native *TcAChE*.

Structure determination and refinement (structure **3**) were carried out essentially as described above for structure **1**. Refinement statistics are given in Table 1. The quality of structure **3** was checked and validated using *PROCHECK*. The effect of UV irradiation on native *TcAChE* was evaluated by computing an error-scaled difference distance matrix between this structure and that refined from a native crystal (**N**) annealed to RT for 9 s but without laser exposure (data not shown).

3. Results

3.1. Photolysis of the NPT-AsCh–*TcAChE* complex

NPT-AsCh is a photolabile cholinergic ligand and can be photolysed by exposure to 266 nm laser light even at temperatures as low as 100 K (Specht *et al.*, 2001). Whether photolysis at 100 K leads to release of AsCh and the free *o*-nitrosotrifluoromethylacetophenone at that temperature or only to formation of an hemiacetal intermediate (Corrie *et al.*, 2003) with an absorption spectrum that closely resembles that of the free *o*-nitrosotrifluoromethylacetophenone remains to be clarified (Bourgeois & Weik, 2005). Photolysis of NPT-AsCh by means of 266 nm laser light can also be achieved in crystals of its complex with *TcAChE* (Fig. 3*a*). However, owing to strong competitive absorption by aromatic residues, photolysis at this wavelength is only efficient if very thin crystals are used ($< 20 \mu\text{m}$ thickness; Fig. 3*b*).

3.2. Binding of NPT-AsCh within the active-site gorge of *TcAChE*

The asymmetric unit of the orthorhombic crystal form of *TcAChE* contains two copies of the protein that associate to form a dimer *via* a four-helix bundle (Greenblatt *et al.*, 2004; Fig. 5*a*), with the association being stabilized by an inter-subunit disulfide bridge that is not visible in the electron-density maps. The monomeric enzyme is composed of two domains, comprising residues 4–305 and 306–535, which face one another across the active-site gorge (Fig. 5*a*). In the following, the results referred to are valid for both monomers unless stated otherwise.

In structure **1** (the unphotolysed NPT-AsCh–*TcAChE* complex), two NPT-AsCh molecules could be assigned with full occupancies to each monomer: one at the CAS and the other at the PAS (Fig. 5*b*). The use of NPT-AsCh instead of NPT-Ch permitted easy location of the As atoms owing to their clear anomalous signal (the $K\alpha$ absorption edge of As is

at 11.8 keV) at the wavelength employed ($\lambda = 0.977 \text{ \AA}$; *i.e.* 12.7 keV). The quaternary arsenium moiety of the NPT-AsCh bound at the CAS (Figs. 5*b* and 9) interacts mainly with Trp84, Phe330 and Glu199 (the distances between the two closest non-H atoms are 3.4, 3.3 and 3.0 \AA , respectively), while its aromatic NPT moiety stacks between the side chains of Phe330, Phe331 and Tyr334 (Fig. 5; the distances between the two closest non-H atoms are 3.3, 3.5 and 3.2 \AA , respectively). The CF_3 group of the NPT moiety of NPT-AsCh faces the acyl pocket, *i.e.* Trp233, Phe288 and Phe290, hence mimicking the methyl group of the acetyl moiety of ACh. A similar binding of a CF_3 group in the acyl pocket was observed in the crystal structure of the complex of *TcAChE* with the transition-state analogue TMTFA (Harel *et al.*, 1996). Apart from the small rotations ($<10^\circ$) undergone by the side chains of Phe330 and Phe331, no conformational changes are observed in the active site upon binding NPT-AsCh.

At the PAS, an NPT-AsCh is seen which is oriented 'upside-down' (Figs. 5*b* and 5*d*) relative to the NPT-AsCh bound at the CAS; hence, the two aromatic NPT moieties of the molecules bound at the PAS and at the CAS interact with each other *via* hydrophobic stacking (the distance between the two closest non-H atoms of their respective aromatic rings is 3.2 \AA). The AsCh moiety of the NPT-AsCh molecule at the PAS points toward the bulk and is mainly stabilized by cation– π interactions with Tyr70 and Trp279 (the distances between the two closest non-H atoms are 3.5 and 3.4 \AA , respectively). The aromatic NPT moiety binds within the gorge, with the CF_3 group in the vicinity of the main-chain atoms of Tyr334 and Gly335 (the distances between each F atom and the closest non-H atom are 3.0, 3.0 and 3.1 \AA , respectively). The two O atoms of the nitro group are at a hydrogen-bonding distance

from Phe288 N (distances of 2.6 and 2.9 \AA). Upon binding of NPT-AsCh at the PAS, the side chain of Tyr70 undergoes a $\sim 20^\circ$ rotation towards the bulk. The r.m.s.d. between this structure and the native structure (PDB code 1w75) is 0.35 \AA (Table 4).

3.3. Control experiments: effects of ART and of UV irradiation at RT on *TcAChE* crystals

Our experimental approach makes use of a 266 nm laser to photocleave NPT-AsCh and of ART to permit expulsion of the released AsCh from the active-site gorge (Fig. 4). Hence, two main controls were needed: (i) a control to address the issue of structural changes that might be induced by ART and (ii) a control to discriminate between conformational changes arising owing to UV damage and those related to NPT-AsCh photolysis and ART.

The effect of ART on the structure of the NPT-AsCh–*TcAChE* complex was investigated by computing error-scaled difference distance matrices (ESDDMs; Schneider, 2000). In such a matrix, positive (red) and negative (blue) peaks indicate increased and reduced distances, respectively, between the C^α atoms of the structures being compared (*i.e.* expansion and contraction of given segments of the structure, respectively). ESDDMs were calculated between the unphotolysed structure obtained after flash-cooling to 100 K (structure **1**) and the two partial models refined using the data set collected after a 9 s ART (structures **2^{GS}** and **2^{AS}**). The partial refinement procedure, carried out after a final model was independently refined and in which one conformer (**2^{AS}**, with an occupancy of 20%) was allowed to change conformation while another one was held fixed (**2^{GS}**, with an occupancy of 80%),

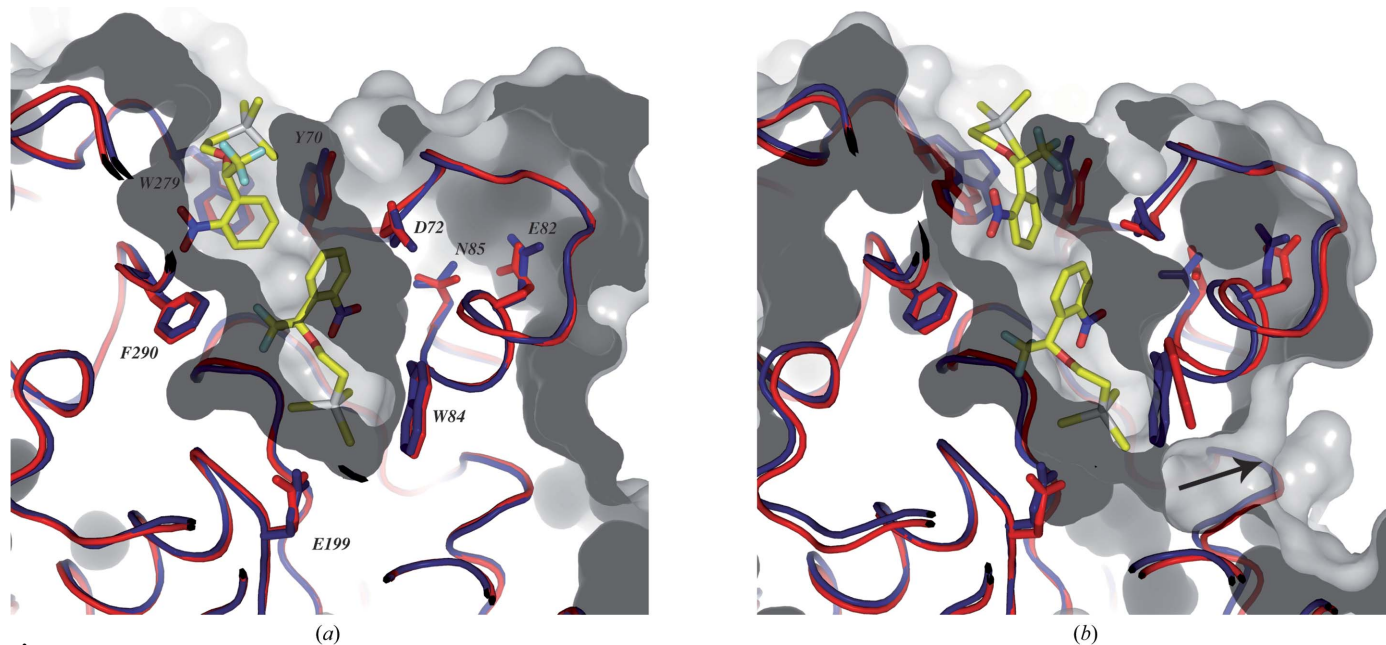


Figure 9 Opening of a backdoor across the gorge wall of the active-site in monomer A. (a) The Connolly surface of structure **2^{AS}** (red C^α trace and sticks), with structure **2^{GS}** (blue C^α trace and sticks) superimposed for comparison. (b) The Connolly surface of structure **4^{AS}** (red C^α trace and sticks), with structure **4^{GS}** being superimposed for comparison (blue C^α trace and sticks). Residues Tyr70, Asp72, Glu82, Met83, Trp84, Asn85, Trp279 and Phe290 are shown as sticks. The arrow indicates the opening of a channel owing to a conformational change of Trp84 in structure **4^{AS}**.

clearly improved the accuracy of the model of structure **2** (Tables 1 and 2). The ESDDM computed between structures **1** and **2^{AS}** (Fig. 6, lower half) is essentially featureless, showing that no striking conformational changes are produced in the NPT-AsCh–TcAChE complex by the ART procedure. Although refinement of structure **2** yielded a higher R_{free} value, only a small loss in diffraction quality was observed with respect to structure **1** (see Table 1), showing that the ART procedure does not damage the crystal. The two NPT-AsCh molecules are found at the same loci and both still display full occupancy. Peaks of $>17\sigma$ are seen for each As atom in the anomalous map of structure **2**, just as for structure **1**. The B -factor values of both the protein and the NPT-AsCh atoms are also very similar in structures **1** and **2**. The r.m.s.d. between structures **1** and **2^{GS}** is 0.23 Å, while that between structures **1** and **2^{AS}** is 0.41 Å (the r.m.s.d. between structures **2^{GS}** and **2^{AS}** is 0.38 Å, with the mean r.m.s.d. among the various structures discussed throughout the paper being 0.30 Å; Table 4).

In order to investigate the effect of UV exposure at RT on TcAChE, a native orthorhombic TcAChE crystal was flash-cooled to 100 K and then brought to RT for 9 s, during the first 5 s of which it was exposed to the 266 nm laser beam (structure **3**; see §2). An ESDDM was calculated between structures **3** and **N** (the native orthorhombic TcAChE crystal annealed to RT for 9 s) and was virtually featureless, indicating that no significant structural changes occur during the 5 s UV irradiation at RT (not shown). It must be noted that no disulfide breakage was observed in structure **3** either in $F_o - F_c$ or in $F_o^3 - F_o^N$ electron-density maps (the R_{merge} between the two data sets was 9%). The r.m.s.d. between structures **3** and **N** is 0.18 Å and that between structure **3** and the native structure is 0.19 Å (Table 4).

3.4. Structure of the NPT-AsCh–TcAChE complex after photolysis of NPT-AsCh at RT

Data for this structure (structure **4**) were collected after flash-cooling to 100 K followed by 9 s ART, during the first 5 s of which the crystal was exposed to the 266 nm laser (see Fig. 4 and §2). This structure was refined using the ‘difference-refinement’ procedure (Fermi *et al.*, 1982; Terwilliger & Berendzen, 1995) to improve the estimates of structural differences with respect to structure **2**. Structure-factor difference amplitudes ($F_o^4 - F_o^2$) were q -weighted (Ursby & Bourgeois, 1997) so as to improve their estimates and to reduce the noise level. Partial refinement was then carried out in which 20% of the structure was allowed to change conformation (structure **4^{AS}**) while the remaining 80% was held fixed (structure **4^{GS}**). The partial refinement strategy and the use of q -weighted structure-factor amplitude differences in the difference refinement improved the quality of structure **4** (Table 2). The results for monomers *A* and *B* are very similar and only those for monomer *A* are presented in the following unless stated otherwise.

The ESDDM between structures **2^{AS}** and **4^{AS}** (Fig. 6, upper half) reveals a clear tendency of the protein to expand upon photolysis of the bound ligand at RT, since most $C^\alpha - C^\alpha$

distances are larger (red pixels in Fig. 6) in structure **4^{AS}** than in structure **2^{AS}**. In fact, the two domains of the enzyme, comprising residues 4–305 and 306–535, which face one another across the active-site gorge (Figs. 1 and 5*a*), move away from each other (Fig. 6, upper half), resulting in a large increase in the volume of the active-site gorge (30% and 35% for monomers *A* and *B*, respectively; Table 5).

The architecture of the active-site gorge is conserved in structure **4^{GS}** relative to structures **1**, **2^{GS}** and **2^{AS}**. Structure **4^{AS}**, however, displays a structure in which the conformation of the active-site gorge has been modified (Figs. 8 and 9). Most residues lining the gorge wall display small backbone movements (not more than a few tenths of an angstrom) with respect to structure **2^{AS}**. The most important backbone deviations concern residues 114–120, 123–128, 336–348 and 437–448. Small side-chain deviations are observed for several residues on the surface. Inside the gorge, noteworthy movements are those of Tyr70, Asp72, Trp84, Tyr114, Tyr121, Leu127, Tyr130, Glu199, Phe288, Phe330 and Tyr442 in both monomers, Val129 and Glu445 in monomer *B* only and Trp279 in monomer *A* only (Figs. 8 and 9).

Difference electron-density maps were calculated between structures **2** and **4** using as Fourier coefficients either $F_o^4 - F_o^2$ (not shown) or $q \times (F_o^4 - F_o^2)$ and the calculated phases of structure **2** (*i.e.* 20% **2^{AS}** and 80% **2^{GS}**). The R_{merge} between the two data sets was 27%. Both yielded strong negative peaks (with only peaks of absolute value $>4\sigma$ being considered significant) for the As atoms of NPT-AsCh at both the CAS and the PAS (Fig. 8). These peaks suggest a decrease in the occupancy by As atoms at both sites. The putative decrease in the occupancies of the NPT-AsCh molecules in structure **4** was further confirmed by the weakness of the anomalous signal of their AsCh moiety. Indeed, only a very small peak is seen at the CAS of monomer *A* when the anomalous map is displayed at 4σ (not shown). A positive peak in the $q \times (F_o^4 - F_o^2)$ difference map is seen in the CAS next to the position of the arsenium moiety in structure **2** (Fig. 8), yet there is no concomitant anomalous signal at the same position or near it (not shown). This positive peak is thus unlikely to correspond to a repositioning of the photocleaved AsCh. Likewise, it seems improbable that it corresponds to a repositioning of the cage moiety, which appears to stay put based on the absence of a substantial negative density at the starting location of the cage. Rather, this positive peak might reveal the binding of a solvent molecule.

The $q \times (F_o^4 - F_o^2)$ difference electron-density map yielded significant peaks in the protein structure. Most importantly, a negative peak is seen at the side chain of Trp84 (-5.4σ) and a positive peak next to it (Fig. 8). A negative peak is seen at the PAS of monomer *B* at the side chain of Trp279 (-4.3σ ; not shown). The main constituents of the PAS, Trp279, Tyr70, Tyr121 and Tyr334, undergo conformational changes in structure **4^{AS}**. In the CAS of structure **4^{AS}**, the side chain of Trp84 moves concertedly with Met83, Tyr130, Tyr442 and Glu445 (Figs. 8 and 9). As a consequence, an opening in the active-site wall is observed that is large enough to allow the passage of a water molecule. In monomer *B*, a channel is also

formed at the same position but is not large enough to allow the passage of a water molecule.

4. Discussion

4.1. Structural changes in the active site of *TcAChE* after photolysis and annealing to RT

Our experimental approach was designed to address the issue of choline exit from the active site of AChE in structural terms and to examine the ‘backdoor’ hypothesis (Ripoll *et al.*, 1993; Gilson *et al.*, 1994). NPT-AsCh was bound within the active site of *TcAChE* and AsCh was ‘uncaged’ by UV-induced photocleavage during a temperature excursion from 100 K to room temperature (RT). Difference electron-density maps suggested a decrease in the occupancy of the photo-freed AsCh at both the CAS and the PAS (Fig. 8). Our results suggest (but do not prove) that a proportion of the AsCh molecules had exited from the CAS after photolysis and annealing to room temperature. No intermediate binding sites for AsCh on its way out of the CAS were observed, despite the fact that use of caged AsCh instead of caged Ch increased the chance of identifying such sites owing to the strong anomalous scattering by the As atom (Peng *et al.*, 1998).

The partial difference refinement of structures **2** and **4** employed here assumes that the crystalline enzyme can adopt two states after photolysis and annealing to room temperature: a ground state and an activated state. Whereas the activated and ground states of structure **2** (control experiment) are similar, the activated state of structure **4** (**4^{AS}**) differs from its ground state. Concomitant with the suggested decrease in the occupancy of the photo-freed AsCh, the two domains of the enzyme, which face one another across the active-site gorge (Morel *et al.*, 1999), moved away from each other in structure **4^{AS}** (Fig. 6), resulting in an increased volume of the active-site gorge (Table 5). The domain movements were not observed when a crystal of the NPT-AsCh–*TcAChE* complex was annealed to RT under the same conditions but without UV irradiation or when a native *TcAChE* crystal was subjected to UV irradiation at RT. These movements are therefore the result of NPT-AsCh photolysis and annealing to room temperature and may have been triggered by the exit of AsCh. This indicates that exit of AsCh occurs *via* the gorge, at least to some extent, at RT.

Most importantly, structure **4^{AS}** shows a deformation of the active-site gorge architecture. In particular, the rotation of the Trp84 side chain towards the bulk in monomer *A* of structure **4^{AS}**, accompanied by side-chain movements of Met83, Val129, Tyr130, Tyr442, Ile444 and Glu445, opens a hole adjacent to the Ch-binding locus of the CAS that is large enough to allow the passage of a water molecule. Evidence for the opening of such a hole is reinforced by difference electron-density maps, in which a pair of positive and negative peaks substantiate the movement of Trp84. We suggest that the observed opening may be a residual trace of an even larger transient opening through which the photo-freed AsCh had escaped: the putative ‘backdoor’ (Gilson *et al.*, 1994). The negative peaks

observed at the cage moieties of the NPT-AsCh molecules are of lower intensity than those observed for the side chain of Trp84 both at the CAS and the PAS. This is consistent with some AsCh molecules exiting the active site *via* a backdoor, leaving the cage still within the gorge.

Our results provide experimental evidence for the existence of a pathway other than the gorge through which at least a fraction of enzymatically generated choline may clear the active site after catalysis. In particular, the observed opening caused by a movement of Trp84 may serve as an alternative route to/from the active site for substrate/products when the principal access route *via* the gorge is obstructed, *e.g.* by binding of FAS (Marchot *et al.*, 1993; Radic *et al.*, 1994, 1995; Eastman *et al.*, 1995). The domain movements observed in our study probably reflect ‘breathing motions’ associated with choline exit *via* the gorge.

4.2. The caged-compound approach in kinetic crystallography of ChEs

X-ray protein crystallography is a very powerful technique for solving macromolecular structures. However, it suffers from the limitation that it displays the time-averaged structure of an ensemble of molecules present in the diffracting volume of the crystal. Consequently, dynamic information cannot usually be assessed. Exploration of the conformational energy landscape of a protein using X-ray crystallography requires the use of experimental tricks to overcome the inherently static nature of crystallographic structures. To date, most successful kinetic crystallography studies have exploited the use of lasers to synchronously and efficiently trigger photo-switchable reactions within light-sensitive proteins and of flash-cooling of the crystal to cryo-trap intermediate states (reviewed by Bourgeois & Royant, 2005). Here, photodissociation of a caged compound by a 266 nm laser was employed which in combination with a ‘freeze–trigger–freeze’ strategy allowed us to address the exit of AsCh from the active site of *TcAChE* in structural terms.

Our approach suffers from at least three principal limitations. Firstly, we employed a 266 nm laser for the UV-induced photolytical reaction of the NPT-caged compound, which displays a maximal absorption cross-section at about this wavelength. However, owing to strong absorption by aromatic residues at 266 nm, less than 10% of the photons remained available for de-caging. Hence, rather thin crystals had to be used in order to maximize the efficiency of photolysis. It is likely that despite a tenfold lower absorption cross-section, the use of near-UV light at 355 nm (and at a similar power) would have allowed more homogeneous photolysis in thicker crystals while minimizing the specific UV damage to protein structures that has been described recently (Neves-Petersen *et al.*, 2002; Vernede *et al.*, 2006; Nanao & Ravelli, 2006). However, such a laser was not available at the time of our study. Further progress using this approach should benefit from the availability of tunable lasers and from the synthesis of caged compounds that dissociate most efficiently upon irradiation at

a wavelength remote from the absorption band of aromatic residues.

The second limitation of our approach relates to the annealing to room temperature (ART) procedure. ART of the crystals was performed to allow the occurrence of molecular motions of the protein, of the photolysis products and of the solvent that might be required for AsCh to exit the active-site gorge. ART procedures demand adequate robustness of the crystals and preliminary characterization of the accessible time range at RT. Other approaches have been used that avoid the need to freeze the sample before light-activation at RT, while preserving crystal integrity. For example, the loop-mounted crystal can be transiently embedded at 277 K in a capillary to avoid evaporation in the course of centring and illumination (Scheidig *et al.*, 1999). However, our approach has the advantage that sophisticated temperature profiles can be applied. In particular, transient annealing, following flash-cooling, to a cryotemperature window in which the solvent has acquired liquid-like properties (Weik, Kryger *et al.*, 2001; Weik, Ravelli *et al.*, 2001; Weik *et al.*, 2005) might unleash some of the motions of both protein and solvent required for a given enzymatic reaction to proceed a step further. Under such conditions and if a high photolysis efficiency of the given caged compound is achievable at cryogenic temperatures, higher resolution structures of intermediate states should be attainable (Ursby *et al.*, 2002).

Another limitation of the method concerns a possible discrepancy between the timescale on which experiments are performed (here seconds) and that on which most biologically relevant conformational changes occur (picoseconds to milliseconds). ART is thus best suited for very slow reactions, such as that referred to above (Scheidig *et al.*, 1999), that occur on the timescale of seconds or minutes. In the case of AChE, photolysis of the caged compound and enzymatic catalysis both occur on the microsecond timescale in solution. However, it is possible that the crystalline state and the presence of a highly viscous solvent slows the AChE catalytic turnover in our experimental conditions by several orders of magnitude (Raves, 1998).

5. Conclusions

We have described a kinetic crystallography approach based on a combination of the photolysis of rationally designed caged compounds with temperature-controlled protein crystallography. It can be used to trigger biologically relevant reactions within crystalline samples, hence allowing structural monitoring of the course of an enzymatic event. In the case of AChE, UV-induced photocleavage of NPT-caged AsCh during a brief annealing of the crystal at room temperature most probably resulted in a fraction of the AsCh molecules being expelled from the active-site gorge of the enzyme. Large-amplitude motions of the domains facing one another across the active-site gorge, as well as the increase in its volume occurring concomitantly with the expulsion of AsCh, suggest that product exit partially took place *via* the top of the gorge under the experimental conditions employed. Confor-

mational changes were also observed in the putative backdoor region, suggesting that exit of Ch after catalysis may occur *via* routes alternative to the gorge.

We warmly thank Lilly Toker and Michal Cohen for purification of TcAChE, and Elspeth Garman, Joanne McCarthy, John McGeehan, J  r  my Ohana, Raimond Ravelli and Xavier Vernede for fruitful discussions and help during data collection. We would like to thank one of the referees who advised us to employ the difference-refinement procedure. We gratefully acknowledge the ESRF for beamtime under long-term projects MX347 and MX438 (radiation damage BAG), and MX387 and MX498 (IBS BAG). We are grateful to Didier Fournier for fruitful discussions, to Mike Sawaya for critical reading of the manuscript and to Juan Fontecilla-Camps for regular access to the X-ray source in his laboratory. We thank James Murray for help in using *ESCFIT* and Chris Miller for providing us with a matrix-plotting Python script. Financial support by the CEA, the CNRS and the UJF is acknowledged, as well as a grant to MW from the Agence Nationale de la Recherche (project No. JC05_45685). JPC was supported by an EMBO short-term fellowship (ASTF230-2006). This study benefited from the US Army Medical and Material Command under Contract No. DAMD17-97-2-7022, the EC Fifth Framework Program on the Quality of Life and Management of Living Resources, the Kimmelman Center for Biomolecular Structure and Assembly (Rehovot, Israel), the Benozziyo Center for Neurosciences and the Kalman and Ida Wolens Foundation. JLS is the Pickman Professor of Structural Biology.

References

- Axelsen, P. H., Harel, M., Silman, I. & Sussman, J. L. (1994). *Protein Sci.* **3**, 188–197.
- Barak, D., Kronman, C., Ordentlich, A., Ariel, N., Bromberg, A., Marcus, D., Lazar, A., Velan, B. & Shafferman, A. (1994). *J. Biol. Chem.* **269**, 6296–6305.
- Bartolucci, C., Perola, E., Cellai, L., Brufani, M. & Lamba, D. (1999). *Biochemistry*, **38**, 5714–5719.
- Bourgeois, D. & Royant, A. (2005). *Curr. Opin. Struct. Biol.* **15**, 538–547.
- Bourgeois, D., Vernede, X., Adam, V., Fioravanti, E. & Ursby, T. (2002). *J. Appl. Cryst.* **35**, 319–326.
- Bourgeois, D. & Weik, M. (2005). *Dynamic Studies in Biology: Phototriggers, Photoswitches and Caged Biomolecules*, edited by M. Goeldner & R. Givens, pp. 410–435. Weinheim: Wiley-VCH.
- Bourne, Y., Radic, Z., Sulzenbacher, G., Kim, E., Taylor, P. & Marchot, P. (2006). *J. Biol. Chem.* **281**, 29256–29267.
- Bourne, Y., Taylor, P. & Marchot, P. (1995). *Cell*, **83**, 503–512.
- Br  nger, A. T., Adams, P. D., Clore, G. M., DeLano, W. L., Gros, P., Grosse-Kunstleve, R. W., Jiang, J.-S., Kuszewski, J., Nilges, M., Pannu, N. S., Read, R. J., Rice, L. M., Simonson, T. & Warren, G. L. (1998). *Acta Cryst.* **D54**, 905–921.
- Bui, J. M., Tai, K. & McCammon, J. A. (2004). *J. Am. Chem. Soc.* **126**, 7198–7205.
- Casida, J. E. & Quistad, G. B. (2005). *Chem. Biol. Interact.* **15**, 277–283.
- Collaborative Computational Project, Number 4 (1994). *Acta Cryst.* **D50**, 760–763.
- Colletier, J.-P., Fournier, D., Greenblatt, H., Sussman, J. L., Zaccai, G., Silman, I. & Weik, M. (2006). *EMBO J.* **25**, 2746–2756.

- Corrie, J. E., Barth, A., Munasinghe, V. R., Trentham, D. R. & Hutter, M. C. (2003). *J. Am. Chem. Soc.* **125**, 8546–8554.
- DeLano, W. L. (2002). *PyMOL*. DeLano Scientific, San Carlos, CA, USA.
- Dundas, J., Ouyang, Z., Tseng, J., Binkowski, A., Turpaz, Y. & Liang, J. (2006). *Nucleic Acids Res.* **34**, W116–W118.
- Eastman, J., Wilson, E. J., Cervenansky, C. & Rosenberry, T. L. (1995). *J. Biol. Chem.* **270**, 19694–19701.
- Eichler, J., Anselmet, A., Sussman, J. L., Massoulie, J. & Silman, I. (1994). *Mol. Pharmacol.* **45**, 335–340.
- Emsley, P. & Cowtan, K. (2004). *Acta Cryst.* **D60**, 2126–2132.
- Enyedy, I. J., Kovach, I. M. & Brooks, B. R. (1998). *J. Am. Chem. Soc.* **120**, 8043–8050.
- Faerman, C., Ripoll, D., Bon, S., Le Feuvre, Y., Morel, N., Massoulie, J., Sussman, J. L. & Silman, I. (1996). *FEBS Lett.* **386**, 65–71.
- Felder, C. E., Harel, M., Silman, I. & Sussman, J. L. (2002). *Acta Cryst.* **D58**, 1765–1771.
- Fermi, G., Perutz, M. F., Dickinson, L. C. & Chien, J. C. (1982). *J. Mol. Biol.* **155**, 495–505.
- Gilson, M. K., Straatsma, T. P., McCammon, J. A., Ripoll, D. R., Faerman, C. H., Axelsen, P. H., Silman, I. & Sussman, J. L. (1994). *Science*, **263**, 1276–1278.
- Golicnik, M., Fournier, D. & Stojan, J. (2001). *Biochemistry*, **40**, 1214–1219.
- Greenblatt, H. M., Dvir, H., Silman, I. & Sussman, J. L. (2003). *J. Mol. Neurosci.* **20**, 369–383.
- Greenblatt, H. M., Guillou, C., Guénard, D., Argaman, A., Botti, S., Badet, B., Thal, C., Silman, I. & Sussman, J. L. (2004). *J. Am. Chem. Soc.* **126**, 15405–15411.
- Hajdu, J. & Andersson, I. (1993). *Annu. Rev. Biophys. Biomol. Struct.* **22**, 467–498.
- Harel, M., Kleywegt, G. J., Ravelli, R. B., Silman, I. & Sussman, J. L. (1995). *Structure*, **3**, 1355–1366.
- Harel, M., Quinn, D. M., Nair, H. K., Silman, I. & Sussman, J. L. (1996). *J. Am. Chem. Soc.* **118**, 2340–2346.
- Harel, M., Schalk, I., Ehret-Sabatier, L., Bouet, F., Goeldner, M., Hirth, C., Axelsen, P. H., Silman, I. & Sussman, J. L. (1993). *Proc. Natl Acad. Sci. USA*, **90**, 9031–9035.
- Kabsch, W. (1993). *J. Appl. Cryst.* **26**, 795–800.
- Karlsson, E., Mbugua, P. M. & Rodriguez-Ithurralde, D. (1984). *J. Physiol. (Paris)*, **79**, 232–240.
- Kleywegt, G. J. (1995). *Jnt CCP4/ESF-EACBM Newsl. Protein Crystallogr.* **31**, 45–50.
- Kleywegt, G. J. & Jones, T. A. (1996). *Acta Cryst.* **D52**, 826–828.
- Kovach, I. M., Qian, N. & Bencsura, A. (1994). *FEBS Lett.* **349**, 60–64.
- Kronman, C., Ordentlich, A., Barak, D., Velan, B. & Shafferman, A. (1994). *J. Biol. Chem.* **269**, 27819–27822.
- Laskowski, R. A., MacArthur, M. W., Moss, D. S. & Thornton, J. M. (1993). *J. Appl. Cryst.* **26**, 283–291.
- Marchot, P., Khelif, A., Ji, Y. H., Mansuelle, P. & Bougis, P. E. (1993). *J. Biol. Chem.* **268**, 12458–12467.
- Millard, C. B. & Broomfield, C. A. (1995). *J. Neurochem.* **64**, 1909–1918.
- Morel, N., Bon, S., Greenblatt, H. M., Van Belle, D., Wodak, S. J., Sussman, J. L., Massoulie, J. & Silman, I. (1999). *Mol. Pharmacol.* **55**, 982–992.
- Mozzarelli, A. & Rossi, G. L. (1996). *Annu. Rev. Biophys. Biomol. Struct.* **25**, 343–365.
- Murshudov, G. N., Vagin, A. A. & Dodson, E. J. (1997). *Acta Cryst.* **D53**, 240–255.
- Nanao, M. H. & Ravelli, R. B. (2006). *Structure*, **14**, 791–800.
- Neves-Petersen, M. T., Gryczynski, Z., Lakowicz, J., Fojan, P., Pedersen, S., Petersen, E. & Petersen, S. B. (2002). *Protein Sci.* **11**, 588–600.
- Nienhaus, G. U., Chu, K. & Jesse, K. (1998). *Biochemistry*, **37**, 6819–6823.
- Peng, L., Nachon, F., Wirz, J. & Goeldner, M. (1998). *Angew. Chem. Int. Ed.* **37**, 2691–2693.
- Quinn, D. M. (1987). *Chem. Rev.* **87**, 955–979.
- Radic, Z., Duran, R., Vellom, D. C., Li, Y., Cervenansky, C. & Taylor, P. (1994). *J. Biol. Chem.* **269**, 11233–11239.
- Radic, Z., Quinn, D. M., Vellom, D. C., Camp, S. & Taylor, P. (1995). *J. Biol. Chem.* **270**, 20391–20399.
- Radic, Z., Reiner, E. & Taylor, P. (1991). *Mol. Pharmacol.* **39**, 98–104.
- Raves, M. L. (1998). PhD thesis. Weizmann Institute of Science, Rehovot, Israel.
- Ripoll, D. R., Faerman, C. H., Axelsen, P. H., Silman, I. & Sussman, J. L. (1993). *Proc. Natl Acad. Sci. USA*, **90**, 5128–5132.
- Rosenberry, T. L. (1975). *Adv. Enzymol. Relat. Areas. Mol. Biol.* **43**, 103–218.
- Royat, A., Carpentier, P., Ohana, J., McGeehan, J., Paetzold, B., Noirclerc-Savoie, M., Verne, X., Adam, V. & Bourgeois, D. (2007). *J. Appl. Cryst.* In the press.
- Scheidig, A. J., Burmester, C. & Goody, R. S. (1999). *Structure*, **7**, 1311–1324.
- Schlichting, I., Almo, S. C., Rapp, G., Wilson, K., Petratos, K., Lentfer, A., Wittinghofer, A., Kabsch, W., Pai, E. F., Petsko, G. A. & Goody, R. S. (1990). *Nature (London)*, **345**, 309–315.
- Schneider, T. R. (2000). *Acta Cryst.* **D56**, 714–721.
- Shen, T., Tai, K., Henchman, R. H. & McCammon, J. A. (2002). *Acc. Chem. Res.* **35**, 332–340.
- Silman, I. & Sussman, J. L. (2005). *Curr. Opin. Pharmacol.* **5**, 293–302.
- Specht, A. & Goeldner, M. (2004). *Angew. Chem. Int. Ed. Engl.* **43**, 2008–2012.
- Specht, A., Ursby, T., Weik, M., Peng, L., Kroon, J., Bourgeois, D. & Goeldner, M. (2001). *Chembiochem*, **2**, 845–848.
- Sussman, J. L., Harel, M., Frolow, F., Oefner, C., Goldman, A., Toker, L. & Silman, I. (1991). *Science*, **253**, 872–879.
- Sussman, J. L., Harel, M., Frolow, F., Varon, L., Toker, L., Futerman, A. H. & Silman, I. (1988). *J. Mol. Biol.* **203**, 821–823.
- Tai, K., Shen, T., Borjesson, U., Philippopoulos, M. & McCammon, J. A. (2001). *Biophys. J.* **81**, 715–724.
- Terwilliger, T. C. & Berendzen, J. (1995). *Acta Cryst.* **D51**, 609–618.
- Theobald, D. L. & Wuttke, D. S. (2006). *Proc. Natl Acad. Sci. USA*, **103**, 18521–18527.
- Ursby, T. & Bourgeois, D. (1997). *Acta Cryst.* **A53**, 564–575.
- Ursby, T., Weik, M., Fioravanti, E., Delarue, M., Goeldner, M. & Bourgeois, D. (2002). *Acta Cryst.* **D58**, 607–614.
- Velan, B., Barak, D., Ariel, N., Leitner, M., Bino, T., Ordentlich, A. & Shafferman, A. (1996). *FEBS Lett.* **395**, 22–28.
- Verne, X., Lavault, B., Ohana, J., Nurizzo, D., Joly, J., Jacquemet, L., Felisaz, F., Cipriani, F. & Bourgeois, D. (2006). *Acta Cryst.* **D62**, 253–261.
- Weik, M., Kryger, G., Schreurs, A. M. M., Bouma, B., Silman, I., Sussman, J. L., Gros, P. & Kroon, J. (2001). *Acta Cryst.* **D57**, 566–573.
- Weik, M., Ravelli, R. B., Silman, I., Sussman, J. L., Gros, P. & Kroon, J. (2001). *Protein Sci.* **10**, 1953–1961.
- Weik, M., Schreurs, A. M. M., Leiros, H.-K. S., Zaccari, G., Ravelli, R. B. G. & Gros, P. (2005). *J. Synchrotron Rad.* **12**, 310–317.
- Wlodek, S. T., Clark, T. W., Scott, L. R. & McCammon, J. A. (1997). *J. Am. Chem. Soc.* **119**, 9513–9522.
- Xu, Y., Shen, J., Luo, X., Silman, I., Sussman, J. L., Chen, K. & Jiang, H. (2003). *J. Am. Chem. Soc.* **125**, 11340–11349.